Seismic and medical ultrasound imaging of velocity and density variations by nonlinear vectorial inverse scattering

Jakobsen, Morten; Xiang, Kui; van Dongen, Koen W.A.

DOI
10.1121/10.0019563

Publication date
2023

Document Version
Final published version

Published in
The Journal of the Acoustical Society of America

MAY 31 2023

Seismic and medical ultrasound imaging of velocity and density variations by nonlinear vectorial inverse scattering

Morten Jakobsen; Kui Xiang; Koen W. A. van Dongen

J Acoust Soc Am 153, 3151 (2023)
https://doi.org/10.1121/10.0019563

JASA ARTICLE

Seismic and medical ultrasound imaging of velocity and density variations by nonlinear vectorial inverse scattering

Morten Jakobsen,[1,a)] Kui Xiang,[1] and Koen W. A. van Dongen[2]
[1]*Centre for Modeling of Coupled Subsurface Dynamics, Department of Earth Science, University of Bergen, Bergen, Norway*
[2]*Department of Imaging Physics, TU Delft, Delft, Netherlands*

ABSTRACT:
We present an iterative nonlinear inverse scattering algorithm for high-resolution acoustic imaging of density and velocity variations. To solve the multi-parameter nonlinear direct scattering problem, the acoustic wave equation for inhomogeneous media in the frequency domain is transformed into a vectorial integral equation of the Lippmann–Schwinger type for the combined pressure and pressure-gradient field. To solve the multi-parameter nonlinear inverse scattering problem, we use the Newton–Kantorovich method in conjunction with matrix-free representations of the Fréchet derivative operators and their adjoints. The approximate Hessian information that is accounted for in our iterative solution of the (nonlinear) multi-parameter inverse scattering problem is essential for the mitigation of multi-parameter cross talk effects. Numerical examples related to seismic and medical ultrasound breast imaging illustrate the performance of the new algorithm for multi-parameter acoustic imaging.
 https://doi.org/10.1121/10.0019563
(Received 23 November 2022; revised 21 April 2023; accepted 7 May 2023; published online 31 May 2023)
[Editor: Steffen Marburg] Pages: 3151–3164

I. INTRODUCTION

There are many similarities between seismic and medical ultrasound imaging.[1–6] In the case of seismic imaging,[7–9] we record waves passing through the Earth to image the Earth's interior in search of anomalies to help in exploring for natural resources. In the case of medical ultrasound imaging,[10–13] we image the interior of the human body to diagnose undesirable anomalies. Seismic and medical ultrasound imaging methods are often applied prior to costly drilling or surgery, respectively, but they can also be applied in time-lapse mode to monitor changes in the medium properties with time. As discussed by Pratt,[1] seismic and medical ultrasound imaging have many similarities, including the concept of anomalies. However, in the case of seismic imaging, we often hope to discover anomalies (e.g., oil or gas), whereas in medical imaging, we often hope to not find anomalies (e.g., tumors).

From the perspective of mathematical physics,[14] both seismic and medical ultrasound imaging can be considered inverse scattering problems (Fig. 1). In mathematical physics, the inverse scattering problem is the problem of determining characteristics of an object, based on data of how it scatters incoming waves or particles. It is the inverse problem to the direct scattering problem, which is to determine how waves or particles are scattered based on the properties of the object. One distinguishes between the linear and nonlinear inverse scattering problems.[15] Whereas an exact solution to the linear inverse scattering problem can be found under ideal circumstances in all dimensions, exact solutions to the (more interesting and relevant) nonlinear inverse scattering problem have only been discovered for one-dimensional systems.[15]

Conventional systems for seismic and medical ultrasound imaging are typically based on linear inverse scattering theory and/or simple approximations that model a part of the wavefield only.[3,11,16,17] However, such approximate and simplified imaging methods give adequate imaging results if and only if the medium is weakly scattering. To deal with strongly scattering media of interest to the geophysical and medical imaging communities, one should ideally use nonlinear inverse scattering theory, which can be equivalent to performing a full-waveform inversion (FWI).[1,5,8,15,18]

By using nonlinear inverse scattering theory in the context of seismic and medical ultrasound imaging, one can potentially obtain images of much higher quality and resolution than the conventional methods that make use of travel time and/or amplitude data only.[8,18,19] However, the nonlinear inverse scattering approach has several practical and fundamental challenges, including its huge computational cost and the sensitivity of the iterative nonlinear inversion results to the starting model.[8] In seismic and medical ultrasound imaging, the density is often assumed to be constant,[4,8] although this can lead to errors in the imaging and interpretation. Multi-parameter nonlinear inverse scattering problem is challenging,[19–23] due to multi-parameter cross talk effects and problems associated with having different parameter classes with different ranges and different effects on the scattered fields.[22,23] We focus here on the simultaneous estimation of velocity and density profiles using a nonlinear inverse scattering approach, namely, the Newton–Kantorovich (NK) method method.[8,9,21,24–26] The novelty of this study is

[a)]Electronic mail: Morten.Jakobsen@uib.no

partially related to the use of a single vectorial integral equation for the direct scattering problem and a matrix-free adjoint vectorial integral equation that accounts for approximate Hessian information in the inverse scattering problem.

The NK method we have developed is based on the minimization of a data mismatch functional using a regularized least squares solution.[8,27,28] Although we use an integral equation rather than a differential equation approach to solve the nonlinear direct scattering problem, the NK method we have developed is essentially a matrix-free multi-parameter distorted Born iterative (DBI) method for the frequency domain FWI method.[14,27–29] This implies that our conventional iterative approach to the nonlinear inverse scattering algorithm is guaranteed to converge if and only if the initial model is sufficiently close to the unknown true model.[29,30]

Weglein *et al*. have criticized conventional iterative methods for solving nonlinear inverse scattering problems and pioneered inverse acoustic scattering methods that do not require an assumed propagation velocity of the medium.[18,31] Their more direct nonlinear inversion approach is based on the Born series solution of the Lippmann– Schwinger equation and a concomitant expansion of the interaction in orders of the data.[18,32] Reversion of the Born series leads to an order-by-order scheme for evaluating the terms of the series representation of the interaction in terms of the measured data.[32] In the inverse scattering series (ISS) method, no *a priori* information about the acoustic medium is in principle required.[32] The finite radius of convergence of the underlying Born series seems to be the only fundamental limitation of the ISS method.[15,32,33] Sub-series of the inverse scattering series corresponding to different sub-tasks of seismic processing have been found to be convergent.[18,33–38] Also, promising attempts to extend the radius of convergence using renormalization techniques have been made.[32,39,40] The ISS method is both interesting and potentially useful for medical ultrasound as well as seismic imaging, but its further development is beyond the scope of the present study.

In this study, we focus on the development of a conventional iterative (local optimization) approach to nonlinear inverse scattering. More specifically, we develop a computationally efficient matrix-free variant of the NK method for multi-parameter nonlinear inverse scattering in acoustic media with variable density and velocity. The outline of this paper is simple. First, we discuss the direct and inverse scattering problems. Then we derive expressions for the linear Fréchet (data sensitivity) operators related to perturbations in the bulk modulus and mass density fields (sufficient to reconstruct the velocity field). Since our goal is to develop a matrix-free traditional iterative nonlinear inverse scattering algorithm, our approach to the inverse scattering problem will be based on a continuous formulation. Our numerical examples are related to seismic and medical ultrasound (breast imaging) and illustrate the fact that we have found an efficient manner to deal with approximate Hessian information in the context of multi-parameter acoustic inversion.

II. THE DIRECT SCATTERING PROBLEM

A. Two coupled integral equations

In the frequency domain, the acoustic wave equation for inhomogeneous media can be written as[41]

$$\nabla \cdot \left(\frac{1}{\rho(\mathbf{x})} \nabla p(\mathbf{x}) \right) + \frac{\omega^2}{\kappa(\mathbf{x})} p(\mathbf{x}) = -s(\mathbf{x}), \tag{1}$$

where $s(\mathbf{x})$ is the (frequency-dependent) volume source density of injection rate, ω is the angular frequency, and $\rho(\mathbf{x})$ and $\kappa(\mathbf{x})$ are the mass density and bulk modulus fields at point $\mathbf{x} \in \mathcal{R}^3$. We have assumed that $p(\mathbf{x})$ is proportional to $e^{i\omega t}$, where ω is the angular frequency.

Under the assumption that the medium is unbounded and the wavefield goes to zero at infinity, the solution of the acoustic wave Eq. (1) is given by[41]

$$p(\mathbf{x}) = \int d^3x' g(\mathbf{x}, \mathbf{x}') s(\mathbf{x}'), \tag{2}$$

where the Green's function $g(\mathbf{x}, \mathbf{x}')$ for the actual inhomogeneous medium satisfies

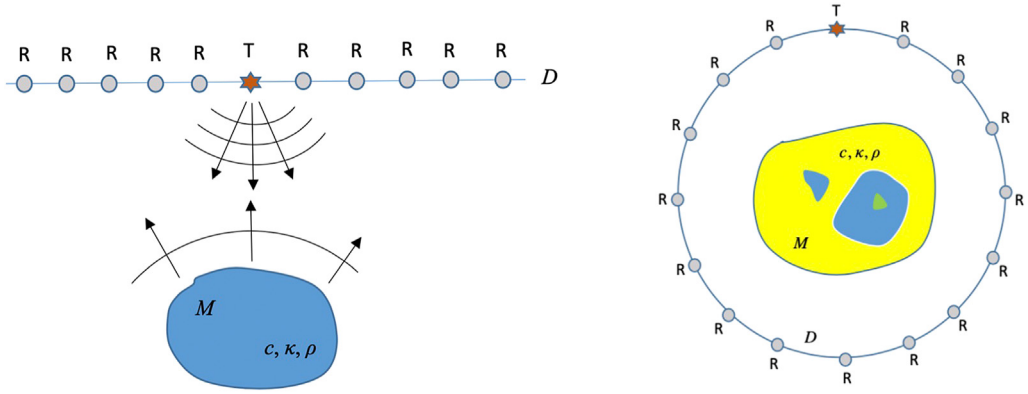

FIG. 1. (Color online) Illustration of inverse scattering problems in the context of (surface) seismic and medical ultrasound (breast) imaging at the top and the bottom, respectively. The scattering object of interest is characterized by bulk modulus, mass density, and speed of sound profiles and surrounded by a set of transducers that can act as sources and receivers. In contrast to medical imaging, seismic imaging is single-sided (unless borehole receivers are also used).

https://doi.org/10.1121/10.0019563

$$\nabla_x \cdot \left(\frac{1}{\rho(\mathbf{x})}\nabla_x g(\mathbf{x},\mathbf{x}')\right) + \frac{\omega^2}{\kappa(\mathbf{x})} g(\mathbf{x},\mathbf{x}') = -\delta(\mathbf{x}-\mathbf{x}'). \quad (3)$$

To derive a volume integral equation for the pressure $p(\mathbf{x})$, we first define the contrast function $m_1(\mathbf{x})$ and $m_2(\mathbf{x})$ by

$$\frac{1}{\kappa(\mathbf{x})} = \frac{1}{\kappa^{(0)}(\mathbf{x})}[1+m_1(\mathbf{x})], \quad \frac{1}{\rho(\mathbf{x})} = \frac{1}{\rho^{(0)}(\mathbf{x})}[1+m_2(\mathbf{x})], \quad (4)$$

where $\kappa^{(0)}(\mathbf{x})$ and $\rho^{(0)}(\mathbf{x})$ are the bulk modulus and mass density fields of an arbitrary homogeneous reference medium. With the definitions in Eq. (4), we ensure that the (normalized) contrast functions $m_1(\mathbf{x})$ and $m_2(\mathbf{x})$ have more or less similar numerical values, which could be helpful when trying to mitigate the problem with multi-parameter cross talk. Then we combine Eqs. (1) and (4) and obtain[19,39,40,42,43]

$$\nabla \cdot \left(\frac{1}{\rho^{(0)}(\mathbf{x})}\nabla p(\mathbf{x})\right) + \frac{\omega^2}{\kappa^{(0)}(\mathbf{x})} p(\mathbf{x}) = -s(\mathbf{x}) - \omega^2 \frac{m_1(\mathbf{x})}{\kappa^{(0)}} p(\mathbf{x}) - \nabla \cdot \left(\frac{m_2(\mathbf{x})}{\rho^{(0)}}\nabla p(\mathbf{x})\right). \quad (5)$$

The last two terms on the right-hand side of Eq. (5) may be referred to as monopole and dipole contrast-sources for bulk modulus and mass density perturbations, respectively.

By using the Green's function theorem and treating the contrast-sources and the primary source $s(\mathbf{x})$ in Eq. (5) in a similar manner, we obtain[19,39,40,42,43]

$$p(\mathbf{x}) = p^{(0)}(\mathbf{x}) + \int_M d^3x' g^{(0)}(\mathbf{x},\mathbf{x}') \times \left[\omega^2 \frac{m_1(\mathbf{x}')}{\kappa^{(0)}} p(\mathbf{x}') + \nabla \cdot \left(\frac{m_2(\mathbf{x}')}{\rho^{(0)}}\nabla p(\mathbf{x}')\right)\right], \quad (6)$$

where M is the model space where the contrast functions are non-zero. In Eq. (6), the background field $p^{(0)}(\mathbf{x})$ is given by

$$p^{(0)}(\mathbf{x}) = \int_\Omega d\mathbf{x}' g^{(0)}(\mathbf{x},\mathbf{x}') s(\mathbf{x}'), \quad (7)$$

where $g^{(0)}(\mathbf{x},\mathbf{x}')$ is the Green's function for the reference medium, which satisfies

$$\nabla_x \cdot \left(\frac{1}{\rho^{(0)}(\mathbf{x})}\nabla g^{(0)}(\mathbf{x},\mathbf{x}')\right) + \frac{\omega^2}{\kappa^{(0)}(\mathbf{x})} g^{(0)}(\mathbf{x},\mathbf{x}') = -\delta(\mathbf{x}-\mathbf{x}'). \quad (8)$$

Explicit analytical formulae for two-dimensional (2D) and three-dimensional (3D) Green's functions in the case of homogeneous acoustic media can be found in the book of Cerveny.[41]

By using partial integration and assuming that all fields within the unbounded medium approach zero at infinity, integral Eq. (6) can be rewritten exactly as

$$p(\mathbf{x}) = p^{(0)}(\mathbf{x}) + \omega^2 \int_M d^3x' g^{(0)}(\mathbf{x},\mathbf{x}') \frac{m_1(\mathbf{x}')}{\kappa^{(0)}} p(\mathbf{x}') - \int_M d^3x' \nabla_{x'} g^{(0)}(\mathbf{x},\mathbf{x}') \cdot \frac{m_2(\mathbf{x}')}{\rho^{(0)}} \nabla p(\mathbf{x}'). \quad (9)$$

By taking the spatial derivative of the fields on both sides of Eq. (9), we find that the gradient vector of the pressure field satisfies the following integral equation:

$$\nabla p(\mathbf{x}) = \nabla p^{(0)}(\mathbf{x}) + \frac{\omega^2}{\kappa^{(0)}} \int_M d^3x' \nabla_x g^{(0)}(\mathbf{x},\mathbf{x}') m_1(\mathbf{x}') p(\mathbf{x}') - \int_M d^3x' \nabla_x \nabla_{x'} g^{(0)}(\mathbf{x},\mathbf{x}') \cdot \frac{m_2(\mathbf{x}')}{\rho^{(0)}} \nabla p(\mathbf{x}'). \quad (10)$$

Explicit analytical expressions for the first- and second-order spatial derivatives of $g^{(0)}$ in the case of a homogeneous reference medium were derived by Xiang *et al.*[43]

B. Equivalent vectorial integral equation

The two coupled integral equations [Eqs. (9) and (10)] for the pressure and pressure gradient fields can be combined into a single vectorial integral equation of the Lippmann–Schwinger type,[43]

$$\boldsymbol{\psi}(\mathbf{x}) = \boldsymbol{\psi}^{(0)}(\mathbf{x}) + \int_M d^3x' \mathbf{G}^{(0)}(\mathbf{x},\mathbf{x}') \cdot \mathbf{V}(\mathbf{x}') \cdot \boldsymbol{\psi}(\mathbf{x}'), \quad (11)$$

where

$$\boldsymbol{\psi}(\mathbf{x}) = [p(\mathbf{x}), \partial_1 p(\mathbf{x}), \partial_2 p(\mathbf{x}), \partial_3 p(\mathbf{x})]^T \quad (12)$$

and

$$\boldsymbol{\psi}^{(0)}(\mathbf{x}) = \left[p^{(0)}(\mathbf{x}), \partial_1 p^{(0)}(\mathbf{x}), \partial_2 p^{(0)}(\mathbf{x}), \partial_3 p^{(0)}(\mathbf{x})\right]^T \quad (13)$$

are four-dimensional state vectors that describes the pressure and the pressure gradient fields in the actual medium and in the heterogeneous background medium, respectively. The 4×4 matrix fields $\mathbf{V}(\mathbf{x})$ and $\mathbf{G}^{(0)}(\mathbf{x},\mathbf{x}')$ in the vectorial integral Eq. (11) are defined by

$$\mathbf{V}(\mathbf{x}) = \begin{bmatrix} \omega^2 \frac{m_1(\mathbf{x})}{\kappa^{(0)}} & 0 & 0 & 0 \\ 0 & \frac{m_2(\mathbf{x})}{\rho^{(0)}} & 0 & 0 \\ 0 & 0 & \frac{m_2(\mathbf{x})}{\rho^{(0)}} & 0 \\ 0 & 0 & 0 & \frac{m_2(\mathbf{x})}{\rho^{(0)}} \end{bmatrix} \quad (14)$$

and

$$\mathbf{G}^{(0)}(\mathbf{x},\mathbf{x}') = \begin{bmatrix} g^{(0)}(\mathbf{x},\mathbf{x}') & -\partial_{1'}g^{(0)}(\mathbf{x},\mathbf{x}') & -\partial_{2'}g^{(0)}(\mathbf{x},\mathbf{x}') & -\partial_{3'}g^{(0)}(\mathbf{x},\mathbf{x}') \\ \partial_1 g^{(0)}(\mathbf{x},\mathbf{x}') & -\partial_1\partial_{1'}g^{(0)}(\mathbf{x},\mathbf{x}') & -\partial_1\partial_{2'}g^{(0)}(\mathbf{x},\mathbf{x}') & -\partial_1\partial_{3'}g^{(0)}(\mathbf{x},\mathbf{x}') \\ \partial_2 g^{(0)}(\mathbf{x},\mathbf{x}') & -\partial_2\partial_{1'}g^{(0)}(\mathbf{x},\mathbf{x}') & -\partial_2\partial_{2'}g^{(0)}(\mathbf{x},\mathbf{x}') & -\partial_2\partial_{3'}g^{(0)}(\mathbf{x},\mathbf{x}') \\ \partial_3 g^{(0)}(\mathbf{x},\mathbf{x}') & -\partial_3\partial_{1'}g^{(0)}(\mathbf{x},\mathbf{x}') & -\partial_3\partial_{2'}g^{(0)}(\mathbf{x},\mathbf{x}') & -\partial_3\partial_{3'}g^{(0)}(\mathbf{x},\mathbf{x}') \end{bmatrix}, \tag{15}$$

respectively. For later reference, we note that the matrix of modified Green's function defined in Eq. (15) satisfies the generalized reciprocity relations $G^{(0)}_{\alpha\beta}(\mathbf{x},\mathbf{x}') = G^{(0)}_{\beta\alpha}(\mathbf{x}',\mathbf{x})$, where $\alpha,\beta = 1,2,3,4$.

When implementing this theory on a computer using a matrix-free approach, the vectorial integral equation is normally rewritten in the form of a linear operator system

$$A\psi = \psi^{(0)}, \tag{16}$$

where the operator A is defined by

$$A\psi \equiv \psi - G^{(0)}V\psi. \tag{17}$$

The linear system (16) is typically solved iteratively using a Krylov subspace method, such as GMRES.[43] Since the (modified) Green's functions for a homogeneous reference medium are translation invariant, one can use the fast Fourier transform (FFT) algorithm to accelerate the convolution of $G^{(0)}$ with various contrast-source terms of the type $V\psi$. As discussed by Xiang *et al.*,[43] the memory requirements and computational cost of this (matrix-free) FFT-based algorithm scale like N and $N\log(N)$, where N denotes the number of grid blocks in a discretized acoustic model.

III. THE INVERSE SCATTERING PROBLEM

A. Multi-parameter NK method

We now turn our attention to the multi-parameter nonlinear inverse scattering problem, that is, the problem of estimating the bulk modulus field $\kappa(\mathbf{x})$ and mass density field $\rho(\mathbf{x})$ from observations of the state vector $\boldsymbol{\psi}(\mathbf{r})$ at the receiver surface.

The parameterization of the acoustic model is important when dealing with multi-parameter inverse scattering problems. In this work, we define a model vector field $\mathbf{m}(\mathbf{x})$ by

$$\mathbf{m}(\mathbf{x}) = [m_1(\mathbf{x}), m_2(\mathbf{x})]^T, \tag{18}$$

where the contrast functions $m_1(\mathbf{x})$ and $m_2(\mathbf{x})$ associated with the bulk modulus and mass density fields were defined in Eq. (4).

Our nonlinear multi-parameter inverse scattering problem is highly ill-posed, so we reformulate it as a local optimization problem, where the goal is to minimize the following error functional:

$$E[\mathbf{m}(\mathbf{x})] = \frac{1}{2}\int d^3r d^3s ||\boldsymbol{\psi}^{(c)}(\mathbf{r},\mathbf{s}) - \boldsymbol{\psi}^{(o)}(\mathbf{r},\mathbf{s})||^2, \tag{19}$$

where $\boldsymbol{\psi}^{(o)}(\mathbf{r},\mathbf{s})$ and $\boldsymbol{\psi}^{(c)}(\mathbf{r},\mathbf{s})$ are the observed and computed values of the wavefield at position $\mathbf{r}$ due to a point source at $\mathbf{s}$. The computed values of the wavefield $\boldsymbol{\psi}^{(c)}(\mathbf{r},\mathbf{s})$ are functionals of the model vector field $\mathbf{m}(\mathbf{x})$, but we suppress this dependency to simplify the notation. In any case, the optimal solution to our inverse scattering problem is defined as the estimate of $\mathbf{m}(\mathbf{x})$ that minimizes the above error functional.

To minimize the error functional (19), we use the DBI method,[25] which is known to be equivalent with the so-called NK method.[14] This implies that the DBI method converges if the initial model is sufficiently close to the (unknown) true model. The DBI (or NK) method involves a linearization of the forward model around a heterogeneous background model. To perform this linearization, we perform a first-order functional Taylor expansion of the computed data $\boldsymbol{\psi}^{(c)}(\mathbf{r},\mathbf{s})$, recorded at receiver position $\mathbf{r}$ due to a source at $\mathbf{s}$, around a heterogeneous background model (equal to the inverted model from the previous iteration),[14]

$$\boldsymbol{\psi}^{(c)}(\mathbf{r},\mathbf{s}) \approx \boldsymbol{\psi}^{(b)}(\mathbf{r},\mathbf{s}) + [\mathcal{F}\delta\mathbf{m}](\mathbf{r},\mathbf{s}), \tag{20}$$

where $\psi^{(b)}(\mathbf{r},\mathbf{s})$ is the field in the background model with model vector field $\mathbf{m}^{(b)}(\mathbf{x})$. We shall come back to the exact definition of the Fréchet derivative operator $\mathcal{F}$. It follows from Eqs. (19) and (20) that

$$E[\mathbf{m}(\mathbf{x})] \approx \frac{1}{2}\int d^3r d^3s ||\Delta\boldsymbol{\psi}(\mathbf{r},\mathbf{s}) + [\mathcal{F}\delta\mathbf{m}](\mathbf{r},\mathbf{s})||^2, \tag{21}$$

where

$$\Delta\boldsymbol{\psi}(\mathbf{r},\mathbf{s}) \equiv \boldsymbol{\psi}^{(b)}(\mathbf{r},\mathbf{s}) - \boldsymbol{\psi}^{(o)}(\mathbf{r},\mathbf{s}) \tag{22}$$

is the vectorial data residual. Thus, we can update the model vector field after each iteration by using

$$\mathbf{m}(\mathbf{x}) = \mathbf{m}^{(b)}(\mathbf{x}) + \delta\mathbf{m}(\mathbf{x}), \tag{23}$$

where $\delta\mathbf{m}$ is the solution to the normal equation,

$$\left[\mathcal{F}^\dagger\mathcal{F}\right]\delta\mathbf{m}(\mathbf{x}) = -\left[\mathcal{F}^\dagger\Delta\boldsymbol{\psi}\right](\mathbf{x}). \tag{24}$$

B. Block structure of the normal equations

The Fréchet derivative operator $\mathcal{F}$ corresponding with the model parameter vector field in Eq. (18) can be expressed in block-matrix form as[23]

$$\mathcal{F} = (\mathcal{F}_1, \mathcal{F}_2), \tag{25}$$

where $\mathcal{F}_1$ and $\mathcal{F}_1$ are associated with variations in the bulk modulus and mass density fields, respectively. By using the above representation of $\mathcal{F}$ in the normal Eq. (24), we obtain

https://doi.org/10.1121/10.0019563

$$\begin{pmatrix} \mathcal{F}_1^\dagger \\ \mathcal{F}_2^\dagger \end{pmatrix} (\mathcal{F}_1, \mathcal{F}_2) \begin{pmatrix} \delta m_1 \\ \delta m_2 \end{pmatrix} = - \begin{pmatrix} \mathcal{F}_1^\dagger \\ \mathcal{F}_2^\dagger \end{pmatrix} \Delta \boldsymbol{\psi}, \tag{26}$$

which is equivalent with[23]

$$\begin{pmatrix} \mathcal{F}_1^\dagger \mathcal{F}_1 & \mathcal{F}_1^\dagger \mathcal{F}_2 \\ \mathcal{F}_2^\dagger \mathcal{F}_1 & \mathcal{F}_2^\dagger \mathcal{F}_2 \end{pmatrix} \begin{pmatrix} \delta m_1 \\ \delta m_2 \end{pmatrix} = - \begin{pmatrix} \mathcal{F}_1^\dagger \\ \mathcal{F}_2^\dagger \end{pmatrix} \Delta \boldsymbol{\psi}. \tag{27}$$

The off diagonal blocks represent the correlations between the sensitivity kernels associated with the parameters of different natures and, hence, reflect the trade-off effects between these parameters. Similarly, the diagonal elements of each sub-matrix provide information of coincident-in-space model parameters of different natures, and the off diagonal elements provide information about the interaction between parameters of different natures in different spatial locations.[23] Incorporating the inverse of the Gauss–Newton approximate Hessian will correct these effects and re-scale the magnitudes of different parameters during the optimization process.[23] This can be regarded as some kind of implicit regularization.

C. Multi-parameter Tikhonov regularization

When solving the normal Eq. (27) using a matrix-free Krylov subspace method, such as GMRES, there is some kind of regularization involved.[25] However, our experience is that some kind of (additional) regularization is always needed for applications to realistic models.[25] There exist a range of different methods that can potentially be used to solve ill-posed nonlinear inverse scattering problems.[8] In this paper, we use a generalized Tikhonov regularization method; that is, we simply add a block-diagonal regularization operator to the left side of the normal Eq. (27) so that we obtain

$$\left[\begin{pmatrix} \mathcal{F}_1^\dagger \mathcal{F}_1 & \mathcal{F}_1^\dagger \mathcal{F}_2 \\ \mathcal{F}_2^\dagger \mathcal{F}_1 & \mathcal{F}_2^\dagger \mathcal{F}_2 \end{pmatrix} + \begin{pmatrix} \lambda_1^2 \mathcal{I} & 0 \\ 0 & \lambda_2^2 \mathcal{I} \end{pmatrix} \right] \begin{pmatrix} \delta m_1 \\ \delta m_2 \end{pmatrix} = - \begin{pmatrix} \mathcal{F}_1^\dagger \\ \mathcal{F}_2^\dagger \end{pmatrix} \Delta \boldsymbol{\psi}, \tag{28}$$

where $\mathcal{I}$ is the identity operator and $\lambda_i, i = 1, 2$ are regularization parameters. There exist a range of different methods for selecting optimal regularization parameters, but most of these methods have been developed under the assumption that the inverse problem is linear and characterized by a single parameter field.[44] In the case of multi-parameter nonlinear inverse problems, the selection of optimal regularization parameters can be based on a combination of theory and heuristic methods. In this paper, we ensure that the ratio between the two regularization parameters remains fixed during the iterative nonlinear inversion process, and we use a variant of the Levenberg–Marquard method to select the optimal value for a single independent regularization parameter.[45] Typically, we start with a relatively large value for the independent regularization parameter and then decrease this gradually with the number of iterations.[8,44] Rather than having a fixed ratio between the two regularization parameters, it is also possible to change the ratio of the two regularizations during the iterative inversion so that one alternating updates the bulk modulus and mass density fields. In any case, having two regularization parameters allows for more flexibility in the attempts to mitigate the effects of multi-parameter cross talk.

IV. FRÉCHET DERIVATIVES AND ADJOINTS

A. Decomposition of the acoustic scattering potential

When dealing with multi-parameter inverse scattering problems in acoustic media, it is convenient to decompose the scattering potential matrix $\mathbf{V}$ in the following manner:[26]

$$\mathbf{V}(\mathbf{x}) = \sum_{p=1}^{2} \mathbf{B}^{(p)} m_p(\mathbf{x}), \tag{29}$$

where

$$\mathbf{B}^{(1)} = \begin{bmatrix} \frac{\omega^2}{\kappa^{(0)}} & 0 & 0 & 0 \\ 0 & 0 & 0 & 0 \\ 0 & 0 & 0 & 0 \\ 0 & 0 & 0 & 0 \end{bmatrix} \quad \mathbf{B}^{(2)} = \begin{bmatrix} 0 & 0 & 0 & 0 \\ 0 & \frac{1}{\rho^{(0)}} & 0 & 0 \\ 0 & 0 & \frac{1}{\rho^{(0)}} & 0 \\ 0 & 0 & 0 & \frac{1}{\rho^{(0)}} \end{bmatrix}. \tag{30}$$

In this way, we separate the tensorial and scalar parts of the scattering potential, which is convenient for the derivation of Fréchet derivative and adjoint operators.

B. The Fréchet derivative operators

The linear Fréchet derivative operator $\mathcal{F}$ represents a mapping from the model space (M) to the data space (D) that can be expressed as

$$\begin{aligned} [F\delta\mathbf{m}](\mathbf{r}) &= \sum_{p=1}^{2} [F_p \delta m_p](\mathbf{r}, \mathbf{s}) \\ &= \sum_{p=1}^{2} \int_M d^3x F_p(\mathbf{r}, \mathbf{x}, \mathbf{s}) \delta m_p(\mathbf{x}), \end{aligned} \tag{31}$$

where $F_p(\mathbf{r}, \mathbf{x}, \mathbf{s})$ is the data sensitivity kernel of the pth Fréchet derivative operator. Physically, the Fréchet derivative represents a linearization of the forward model around a heterogeneous background model (equal to the inverted model from a previous iteration). To perform this linearization, we use the distorted Born approximation (see Appendix A). This leads to the following expression for the data sensitivity kernels:

$$F_p(\mathbf{r}, \mathbf{x}, \mathbf{s}) = \mathbf{G}^{(b)}(\mathbf{r}, \mathbf{x}) \cdot \mathbf{B}^{(p)} \cdot \boldsymbol{\psi}^{(b)}(\mathbf{x}, \mathbf{s}). \tag{32}$$

The above expression for $[\mathcal{F}_p \delta m_i](\mathbf{r})$ requires an update of the background medium Green's function, and its spatial

derivatives after each iteration. Since this is an extremely costly process, we prefer to use an equivalent (FFT-friendly) expression that only involves the Green's function for the homogeneous reference medium.

Essentially generalizing the ideas of Hesford *et al.*[25] to the multi-parameter case, we now make use of the physical interpretation of the Green's function $\mathbf{G}^{(b)}(\mathbf{r},\mathbf{x})$ for the heterogeneous background medium and find that the action of the operator $[\mathcal{F}_i\delta m_i](\mathbf{r},\mathbf{s})$ is equal to an auxiliary four-dimensional vector field $\boldsymbol{\psi}_J^{(p)}(\mathbf{r},\mathbf{s})$ that satisfies the data equation

$$\boldsymbol{\psi}_J^{(p)}(\mathbf{r},\mathbf{s}) = \boldsymbol{\psi}_J^{(0,p)}(\mathbf{r},\mathbf{s}) + \int_M d^3x \mathbf{G}^{(0)}(\mathbf{r},\mathbf{x}) \cdot \mathbf{V}^{(b)}(\mathbf{x}) \cdot \boldsymbol{\psi}_J^{(p)}(\mathbf{x},\mathbf{s}), \tag{33}$$

where $\boldsymbol{\psi}_J^{(p)}(\mathbf{x},\mathbf{s})$ is the solution to the corresponding domain equation

$$\boldsymbol{\psi}_J^{(p)}(\mathbf{x},\mathbf{s}) = \boldsymbol{\psi}_J^{(0,p)}(\mathbf{x},\mathbf{s}) + \int_M d^3x' \mathbf{G}^{(0)}(\mathbf{x},\mathbf{x}') \cdot \mathbf{V}^{(b)}(\mathbf{x}') \cdot \boldsymbol{\psi}_J^{(p)}(\mathbf{x}',\mathbf{s}). \tag{34}$$

Here, $\boldsymbol{\psi}_J^{(0,p)}(\mathbf{x},\mathbf{s})$ is defined by

$$\boldsymbol{\psi}_J^{(0,p)}(\mathbf{x},\mathbf{s}) = \int_M d^3x' \mathbf{G}^{(0)}(\mathbf{x},\mathbf{x}') \cdot \mathbf{J}^{(p)}(\mathbf{x}',\mathbf{s}), \tag{35}$$

where $\mathbf{J}^{(p)}(\mathbf{x}',\mathbf{s}) = \mathbf{B}^{(p)} \cdot \boldsymbol{\psi}^{(b)}(\mathbf{x}',\mathbf{s})\delta m_p(\mathbf{x}')$ is the contrast-source corresponding to perturbations in the pth model parameter field. Thus, to find the variation in the wavefield due to simultaneous perturbations in $\kappa(\mathbf{x})$ and $\rho(\mathbf{x})$, we simply solve a vectorial integral equation of the Lippmann–Schwinger type using the FFT-Krylov iterative method, with the auxiliary current density source $\mathbf{J}^{(p)}(\mathbf{x}',\mathbf{s})$ instead of the physical source.

C. The adjoint of the Fréchet derivative operators

The adjoint operator $\mathcal{F}^\dagger$ represents a mapping from the data space (D) to the model space (M). By using the definition of the adjoint of an arbitrary operator, we show in Appendix B that the adjoints of the operators $\mathcal{F}_p$ are given by

$$\left[\mathcal{F}_p^\dagger \Delta\boldsymbol{\psi}\right](\mathbf{x}) = \left[\boldsymbol{\psi}^{(a)}(\mathbf{x}) \cdot \mathbf{B}^{(p)} \cdot \boldsymbol{\psi}^{(b)}(\mathbf{x})\right]^*, \tag{36}$$

where the adjoint wavefield $\boldsymbol{\psi}^{(a)}$ is given by

$$\boldsymbol{\psi}^{(a)}(\mathbf{x}) \equiv \int_D d^3r d^3s \mathbf{G}^{(b)}(\mathbf{x},\mathbf{r}) \cdot \Delta\boldsymbol{\psi}(\mathbf{r},\mathbf{s}). \tag{37}$$

The above expressions for the adjoints of the operators $\mathcal{F}_p$, $p=1$, 2 also involve the updating of the background medium Green's function after each iteration. Generalizing the adjoint integral equation method of Hesford *et al.*[25] to the multi-parameter case, we make use of the physical interpretation of $\mathbf{G}^{(b)}(\mathbf{r},\mathbf{x})$ and find that the adjoint wavefield is given by

$$\boldsymbol{\psi}^{(a)}(\mathbf{x}) = \boldsymbol{\psi}^{(a,0)}(\mathbf{x}) + \int_M d^3x' \mathbf{G}^{(0)}(\mathbf{x},\mathbf{x}') \cdot \mathbf{V}^{(b)}(\mathbf{x}') \cdot \boldsymbol{\psi}^{(a)}(\mathbf{x}') \tag{38}$$

and

$$\boldsymbol{\psi}^{(a,0)}(\mathbf{x}) = \int_D d^3r d^3s \mathbf{G}^{(0)}(\mathbf{x},\mathbf{r}) \cdot [\Delta\boldsymbol{\psi}(\mathbf{r},\mathbf{s})]^*. \tag{39}$$

Essentially similar to the adjoint method used in regular FWI but based on an integral equation formulation, we can compute the action of the adjoint operators $\mathcal{F}_p$ on the data residual vector by solving two vectorial forward problems: First, we solve a vectorial Lippmann–Schwinger equation for $\boldsymbol{\psi}^{(b)}$ using the real source. Then we solve for a similar vectorial Lippmann–Schwinger equation for the adjoint field $\boldsymbol{\psi}^{(a)}$ using the complex-conjugate of the data residual $\boldsymbol{\psi}(\mathbf{r},\mathbf{s})$ observed (for each source) at the receiver surface as the source term.

V. NUMERICAL EXAMPLES

A. Seismic imaging example

To test the presented multi-parameter inverse scattering method and especially its ability to deal with multi-parameter cross talk effects, we first inverted synthetic seismic waveform data associated with the seismic model shown in Fig. 2. The left column of images in Fig. 2 shows the spatial distribution of sources and receivers in conjunction with the bulk modulus and mass density fields of the true model, respectively. In this example, we employ 32 sources and 128 receivers that are uniformly distributed at the top of the model. The right column of images in Fig. 2 shows the initial model of the bulk modulus and mass density fields we used at the first iteration of the iterative nonlinear inverse scattering method. The initial models were constructed from the true models by employing a Gaussian averaging window with an averaging length equal to 8 grid blocks.

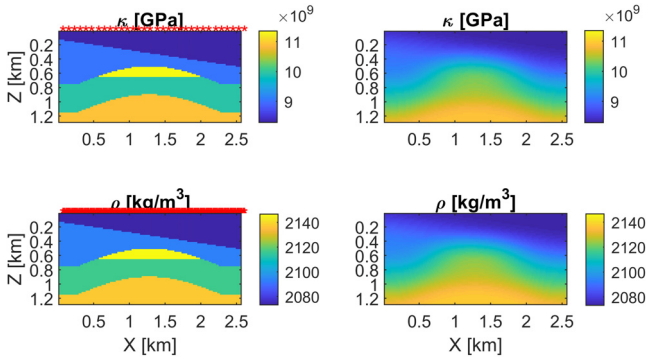

FIG. 2. (Color online) Synthetic seismic model. The upper and lower panels in the left column show the bulk modulus field with the sources and the mass density field with the receivers, respectively. The upper and lower panels in the right column show the corresponding initial models used for nonlinear inverse scattering.

https://doi.org/10.1121/10.0019563

In applications of inverse scattering or FWI methods to real seismic waveform data, the initial model is typically constructed from migration velocity analysis and/or the analysis of seismic travel times and/or amplitudes. In any case, our local optimization approach to multi-parameter nonlinear inverse scattering generally requires a good initial model for convergence. To generate the synthetic measurement data, we solved the vectorial integral Eq. (11) using a FFT-based GMRES algorithm. We employed a Ricker wavelet source with a centre frequency of 10 Hz (see Fig. 3), and space and time were discretized using step sizes of $\Delta x = 20$ m and $\Delta t = 0.0033$ s, respectively.

The temporal sampling interval Δt was selected in accordance with standard Nyquist sampling theory.[46] To minimize the numerical errors associated with a discretization of the volumetric scattering integrals, the spatial sampling interval Δx should be chosen significantly smaller than the smallest seismic or acoustic wavelength. Since our implementation involves the FFT algorithm, one can also use Nyquist sampling theory to determine Δx, albeit with spatial frequencies and wavelengths rather than temporal ones. In any case, the selection of Δx is closely related to the seismic or acoustic imaging resolution. Typically, we ensure that Δx is at least four times smaller than the dominant (or smallest) wavelength., which is often regarded as the resolution limit for FWI.[29] To account for the singularity of the Green's function, we implemented its weak form that is obtained by computing its spherical mean.[42,47–49] The spherical mean approach can in principle also be used to compute so-called correction factors for non-singular cells, for even more accurate spatial discretization.[49]

To avoid being trapped in a local minimum of the data mismatch function, we inverted the synthetic acoustic waveform data associated with the seismic tomography model using the well-known frequency-hopping method. In this multi-scale regularization method, we start with the lowest available frequency and gradually invert higher and higher

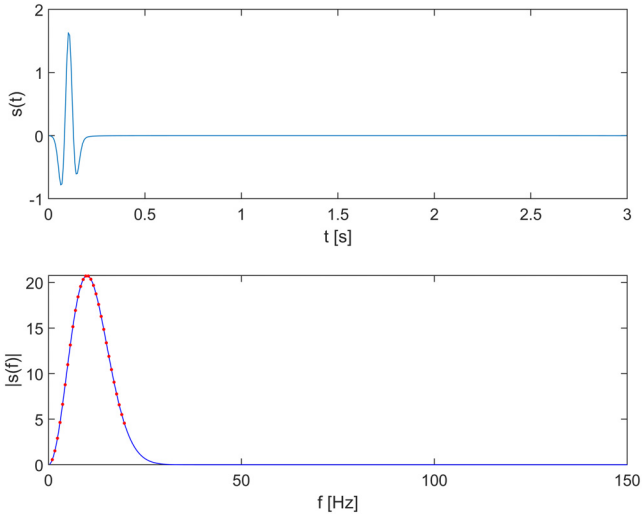

FIG. 3. (Color online) Excitation profile in time and frequency domain used in the numerical example related to seismic imaging.

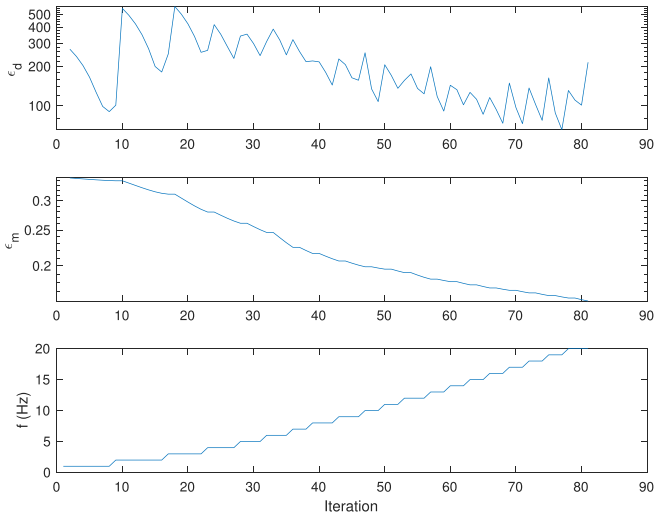

FIG. 4. (Color online) Behavior of the iterative NK method we use to solve the nonlinear multi-parameter inverse scattering problem in the case of the synthetic seismic model. The top and middle panels show the relative residual data and model errors as functions of the number of iterations, respectively. The bottom panel provides information about how many iterations were used at each frequency in the frequency-hopping strategy. The initial value of the regularization parameter λ_1 associated with perturbations in the bulk modulus field was 10^2, and we reduced this value by 10% after each iteration. The corresponding value of λ_2 associated with perturbations in the mass density field was equal to $\lambda_2 = 5\lambda_1$.

frequency components, with the inverted model from a previous frequency as the starting model for the inversion of the current frequency.

Figure 4 illustrates the behavior of the NK method when it is used in conjunction with the frequency-hopping method. The upper and middle plots in Fig. 4 show how the residual data error ϵ_d and the normalized difference between the true and inverted model vectors ϵ_m decrease monotonically with the number of iterations. The lower plot in Fig. 4 provides information about how many iterations were involved at each frequency before full-filling the stopping criterion. We terminated the iterations at each frequency as soon as ϵ_d started to increase or when the maximum number of iterations was reached.

The multi-parameter inverse scattering results for the seismic model are shown together with the true model in Fig. 5. These inversion results illustrate the problem with multi-parameter cross talk that the NK method is able to deal with in a partially successful manner. The fact that the NK method takes into account approximate Hessian information during the iterative inversion process helps to balance the contributions of the bulk modulus and mass density perturbations on the scattered field data. Note that we have also shown the true and inverted acoustic wave speeds $c(\mathbf{x})$, which were obtained from the relevant bulk modulus and mass density fields by using $c(\mathbf{x}) = \sqrt{\kappa(\mathbf{x})/\rho(\mathbf{x})}$.

B. Ultrasound breast imaging example

Figure 6 shows a realistic acoustic model of a cancerous breast based on MR data from a clinical study. This model

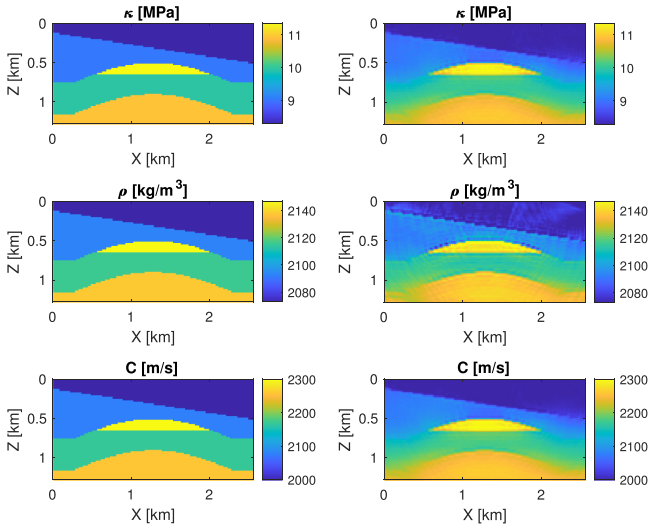

FIG. 5. (Color online) Multi-parameter inverse scattering results for the synthetic seismic model based on our matrix-free implementation of the NK method. The left column shows the true bulk modulus, mass density, and speed of sound profiles; the right column shows the inverse scattering reconstruction using synthetically generated pressure field data. Note that the bulk modulus and mass density fields are independent components of the model parameter vector field involved in the nonlinear inverse scattering, whereas the velocity field is computed from the inverted bulk modulus and mass density fields.

of the bulk modulus and mass density profiles was used to test our multi-parameter inverse scattering algorithm under more realistic conditions. The left and right parts of Fig. 6 also show the spatial distribution of sources and receivers, respectively. As one can see, we employ 32 sources and 64 receivers that are located in a circle in the water tank surrounding the cancerous breast. In our numerical solution to the multi-parameter direct scattering problem, space and

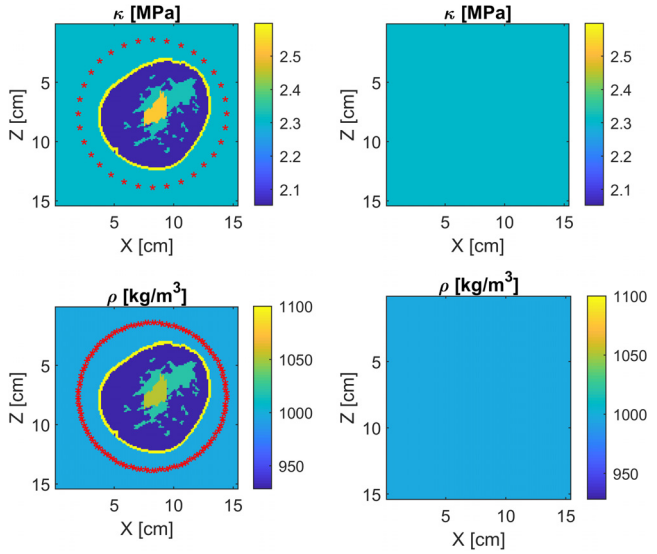

FIG. 6. (Color online) Synthetic ultrasound model based on a cancerous breast based on MR data. The upper and lower panels in the left column show the bulk modulus field with the sources and the mass density field with the receivers, respectively. The upper and lower panels in the right column show the corresponding initial models used for nonlinear inverse scattering.

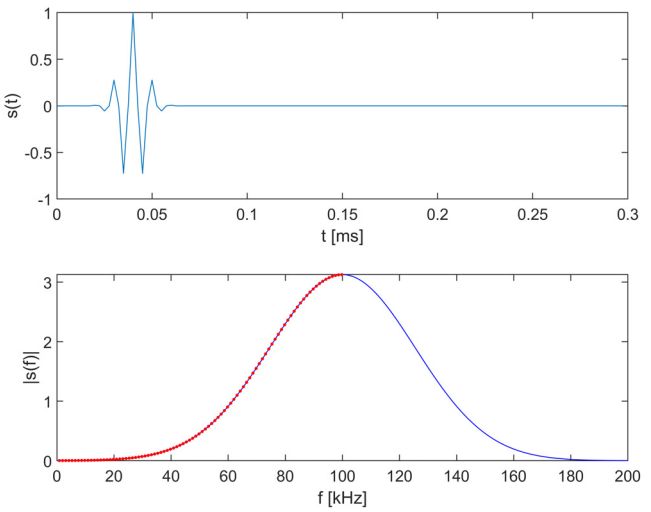

FIG. 7. (Color online) Excitation profile in time and frequency domain used in the numerical experiment related to medical ultrasound breast imaging.

time are discretized using step sizes of $\Delta x = 1.2$ mm and $\Delta t = 2.5$ μs, respectively.

The source wavelet used for probing the wavefield is shown in Fig. 7; a Gaussian modulated pulse with a centre frequency $f_0 = 10$ kHz. Although the bandwidth of the signal is representative of medical ultrasound, its centre frequency is relatively low. Following Taskin *et al.*,[22] this is done to avoid cycle skipping as well as to be able to handle the large acoustic contrast during the inversion. The frequency components used for the inversion are indicated by the red dots. Due to the low centre frequency of the employed source wavelet, attenuation by absorption can be

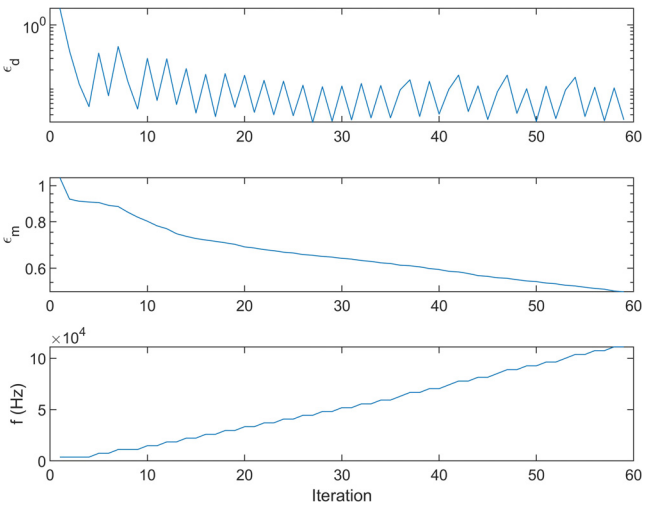

FIG. 8. (Color online) Behavior of the iterative NK method we use to solve the nonlinear multi-parameter inverse scattering problem in the case of the synthetic ultrasound model of a cancerous breast. The top and middle panels show the relative residual data and model errors as functions of the number of iterations, respectively. The bottom panel provides information about how many iterations were used at each frequency in the frequency-hopping strategy. The initial value of the regularization parameter λ_1 associated with perturbations in the bulk modulus field was 10^2, and we reduced this value by 10% after each iteration. The corresponding value of λ_2 associated with perturbations in the mass density field was equal to $\lambda_2 = 5\lambda_1$.

https://doi.org/10.1121/10.0019563

neglected.[22] To avoid being trapped in a local minimum of the data mismatch function, we inverted the synthetic acoustic waveform data associated with the more realistic model of a cancerous breast using the frequency-hopping method described above. Figure 8 illustrates the behavior of the NK method when it is used in conjunction with the frequency-hopping method for the more realistic acoustic model in Fig. 6.

The multi-parameter inverse scattering results for the model of a cancerous breast are shown together with the true model in Fig. 9. Again, we have shown the true and inverted speed of sound profiles that can be computed from the corresponding bulk modulus and mass density profiles. As one can see in Fig. 9, the match between the inverted and true profiles for the bulk modulus, mass density, and wavespeed is relatively good. Although the spatial variations in the different model parameter are relatively complicated, the multi-parameter cross talk appears to be not too challenging for our nonlinear inverse scattering approach. In any case, the fact that we can now reconstruct the mass density in addition to the bulk modulus (or velocity) fields means that one can in principle perform a more detailed characterization of the different tumors involved in ultrasound breast imaging. This is because different types of tumors correspond to different combinations of the three parameter fields we have shown in our numerical experiments, and by reconstructing all these three acoustic model parameter fields from the ultrasound waveforms, one can answer more detailed questions about the condition of a cancerous breast.

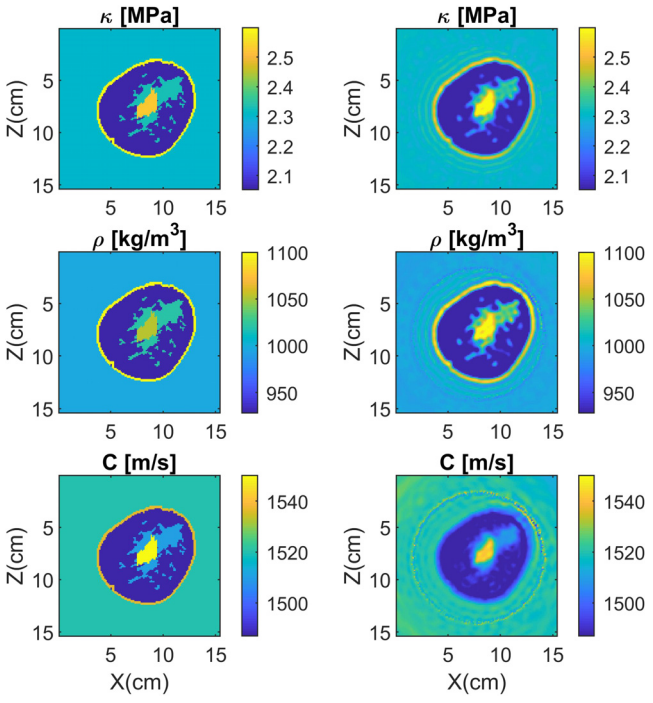

FIG. 9. (Color online) Multi-parameter inverse scattering results for the synthetic ultrasound model with a cancerous breast based on a matrix-free implementation of the NK method. The left column shows the true bulk modulus, mass density, and speed of sound profiles; the right column shows the corresponding inverse scattering reconstruction. Again, the bulk modulus and mass density fields are independent components of the model parameter vector field involved in the nonlinear inverse scattering, whereas the velocity field is computed from the inverted bulk modulus and mass density fields.

VI. DISCUSSION

Although the acoustic test models we employed in Sec. V are fairly realistic, they are not optimal when it comes to the illustration of multi-parameter cross talk effects. The reason for this is that the bulk modulus and mass density fields have the same spatial variations and are correlated to some degree. To better understand the effects of multi-parameter cross talk in the contexts of seismic and medical ultrasound imaging, we have therefore performed some additional numerical experiments based on synthetic acoustic waveform data for more artificial acoustic models where the variations in the bulk modulus and mass density are completely independent and occur at different spatial locations.

Figure 10 shows the artificial seismic model we have used to study the effects of multi-parameter cross talk in the context of seismic imaging. The upper and lower parts of the left column of Fig. 10 show the variation in the bulk modulus and the mass density as well as the source and receiver locations, respectively. The upper and lower parts of the right column of Fig. 10 show the (homogeneous) initial models of the bulk modulus and mass density fields used in the inversion. Clearly, one can see that the perturbations in the bulk modulus and mass density fields relative to a homogeneous background medium are non-zero at different spatial locations, and they are correlated in the middle. We use the same source parameters and grid-size as in the numerical experiment associated with Figs. 2 and 3.

Figure 11 shows reconstructed bulk modulus, mass density, and speed of sound profiles obtained by using the NK method to invert a set of synthetic seismic waveform data for the artificial seismic model in Fig. 10. Clearly, the match between the true and inverted models is very good, although one can see some artefacts on the reconstructed density and speed of sound profiles related to multi-parameter cross talk.

Figure 12 shows similar inversion results obtained by performing the inversion using the conjugate gradient (CG)

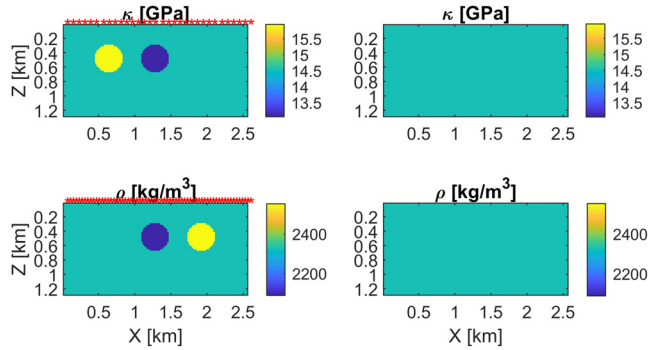

FIG. 10. (Color online) Seismic model designed to investigate the effects of multi-parameter cross talk on the inversion results. The left and right columns of panels show the true model and the initial model, respectively. The locations of the receivers and sources are indicated on the true bulk modulus and mass density models, respectively. The excitation profile used in this numerical experiment is shown in Fig. 3.

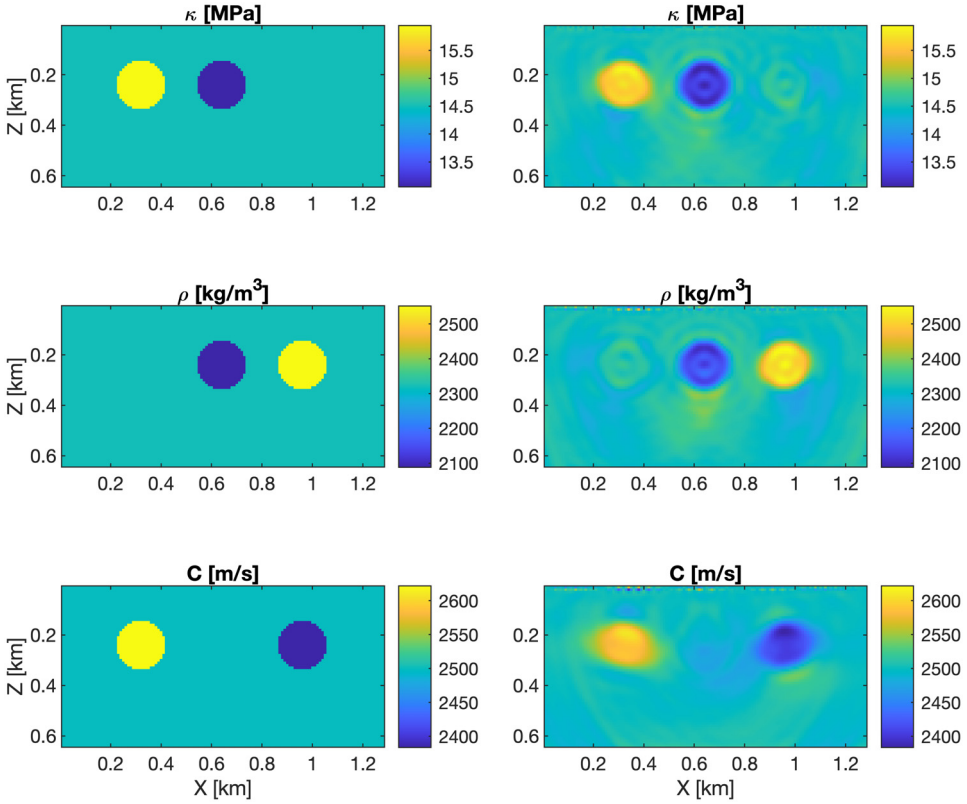

FIG. 11. (Color online) Seismic inversion results for the cross talk model in Fig. 10 obtained using the NK method. The left and right columns of panels show the true and inverted models, respectively.

method (Appendix C) instead of the NK method, but keeping all other parameters fixed. By comparing Fig. 12 with Fig. 11, we can see that inverted results of the CG method are less good than those of the NK method. However, the CG method is faster than the NK method, suggesting that it may sometimes be a good alternative. In any case, both the NK method and the CG method employ the same expressions for the Fréchet derivative and the adjoint operators.

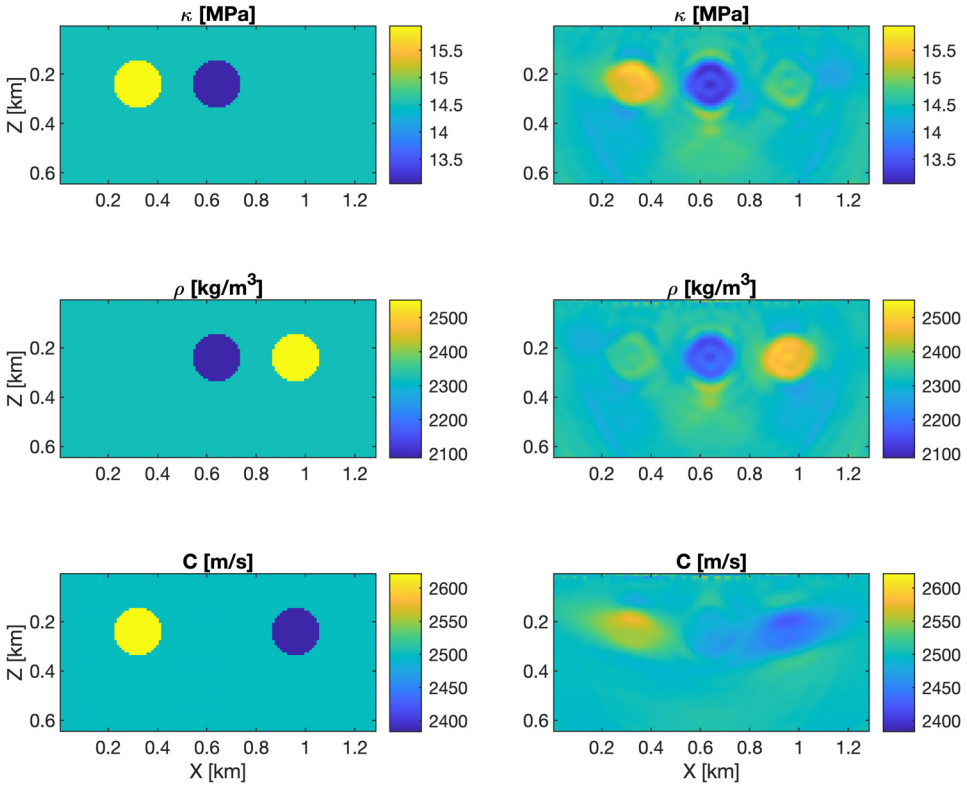

FIG. 12. (Color online) Seismic inversion results for the cross talk model in Fig. 10 obtained using the CG method. The left and right columns of panels show the true and inverted models, respectively.

https://doi.org/10.1121/10.0019563

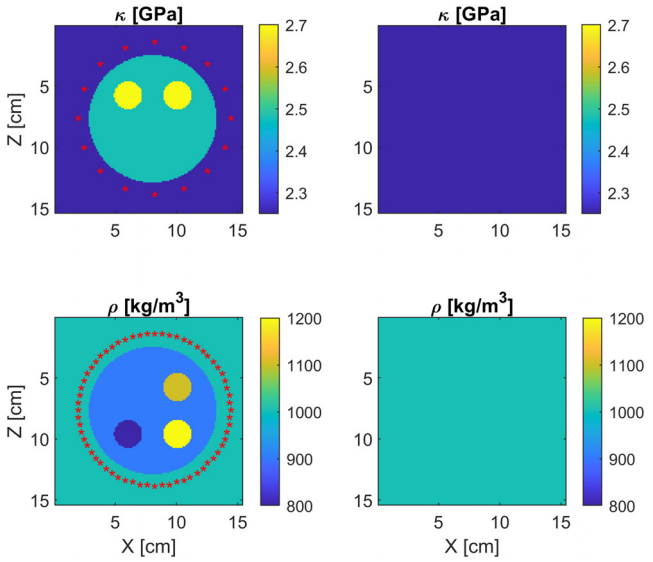

FIG. 13. (Color online) Ultrasonic model designed to investigate the effects of multi-parameter cross talk on the inversion results. The left and right columns of panels show the true model and the initial model, respectively. The locations of the receivers and sources are indicated on the true bulk modulus and mass density models, respectively. The excitation profile used in this numerical experiment is shown in Fig. 7.

Figure 13 shows the artificial ultrasound breast phantom model we have designed to study effects of multi-parameter cross talk in the context of medical ultrasound imaging. The upper and lower parts of the left column of Fig. 13 show the variations in the bulk modulus and the mass density as well as the receiver and source locations, respectively. The upper and lower parts of the right column of Fig. 13 show the (homogeneous) initial models of the bulk modulus and mass density fields we have used in the inversion, respectively. Again, one can see that the spatial variations in the bulk modulus and mass density fields are completely uncorrelated. We use the same source parameters and grid-size as in the numerical experiment associated with Figs. 6 and 7.

Figure 14 shows reconstructed bulk modulus, mass density, and speed of sound profiles obtained using the NK method to invert a set of synthetic ultrasound waveform data for the artificial ultrasound breast phantom model in Fig. 13. Again, the match between the true and inverted models is very good, although some artefacts can again be seen. The effects of multi-parameter cross talk now appear to be smaller than in the corresponding seismic case, and we think this is due to the fact that the ultrasonic source-receiver configuration allows for a more complete illumination, since the sources and receivers are completely surrounding the object of interest.

Figure 15 shows similar inversion results obtained by performing the inversion using the CG method instead of the NK method, but keeping all other parameters fixed. From Figs. 15 and 14, we can see that the inverted results of the NK method are better than those of the CG method.

Although the CG method is a gradient-based optimization method that does not explicitly account for approximate Hessian information and does not involve any regularization

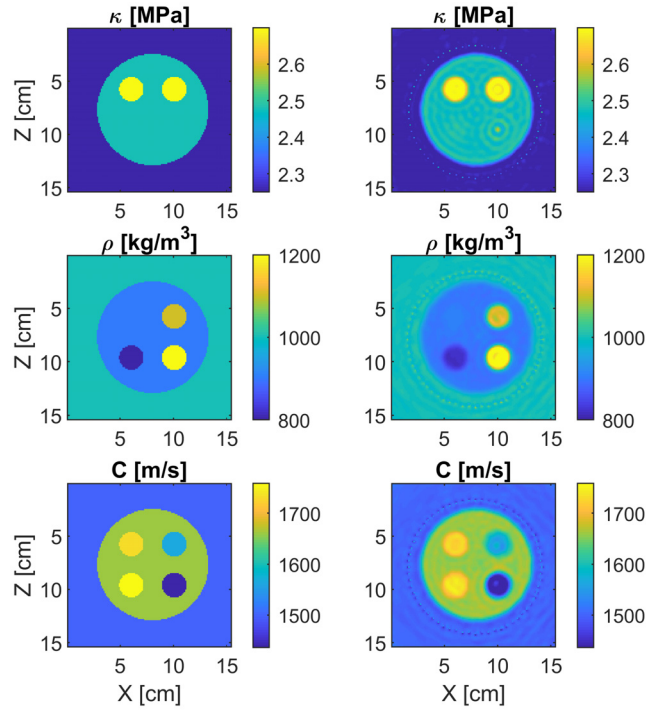

FIG. 14. (Color online) Medical ultrasound inversion results obtained using the NK method.

parameters, it was a little surprising to see that the CG method performed nearly equally as well as the NK method. In any case, our multi-parameter implementation of the CG method is based on the same vectorial integral equation formulation and employs the same expressions for the Fréchet derivative and the adjoint as the NK method derived in this

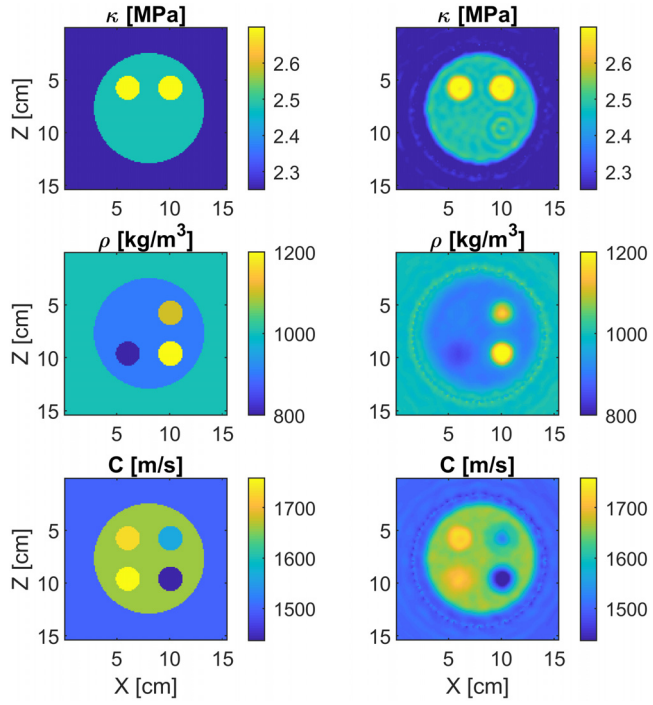

FIG. 15. (Color online) Medical ultrasound inversion results obtained using the CG method.

study. Therefore, most of the theory in this paper is equally relevant for CG- and NK-based implementations of this traditional iterative approach to multi-parameter nonlinear inverse scattering.

VII. CONCLUDING REMARKS

We have generalized an existing NK method based on the scalar wave equation, so that it can be used for nonlinear inverse scattering in acoustic media with variable mass density and bulk modulus, used to reconstruct the velocity profile. This is important since the density carries additional information about the nature of the anomalies associated with seismic and medical ultrasound imaging. The results of a series of numerical experiments performed in this study suggest it is indeed possible to perform a simultaneous inversion of acoustic waveform data for the bulk modulus and mass density field. The multi-parameter DBI algorithm we have developed is completely matrix-free, in the sense that we avoid forming and updating the Green's function for the background medium after each iteration. Instead, we employ an adjoint integral equation method that allows us to take into account approximate Hessian information essential for the mitigation of multi-parameter cross talk effects in an efficient manner.

The starting point for our theoretical derivations was the acoustic wave equation for media with variable mass density and bulk modulus. In the medical ultrasound imaging community, it is generally accepted that the acoustic wave equation with variable density is very good starting point for the development of algorithms for multi-parameter nonlinear inverse scattering algorithms, at least if the region of interest is made of soft matter (e.g., a cancerous breast). In the seismic imaging community, however, researchers agree that the medium should in principle be assumed to act like an elastic solid that supports the propagation of shear waves as well as compressional waves. However, it is still common to use the acoustic approximation to simplify mathematical derivations and to reduce the computational cost associated with large-scale seismic modeling and FWI.[29]

Different researchers in the seismic imaging community seem to have different opinions about the value of imaging algorithms based on the acoustic approximation. We agree with Weglein *et al.* that it does not always make sense to perform a FWI if one ignores the important effects of shear waves. However, it makes sense to use the acoustic approximation when introducing new ideas and concepts. Also, we think it is interesting that what is considered a relatively crude approximation by the seismic community can be highly relevant for medical ultrasound breast cancer detection and characterization. In any case, a generalization of the current work based on the anisotropic elastic wave equation [Eq. (26)] that could potentially be useful for ultrasound imaging of porous and fractured bone structures, the skull and the human brain,[12] as well as seismic imaging and reservoir characterization, is currently under development.

ACKNOWLEDGMENTS

M.J. would like to acknowledge support from VISTA CSD at the University of Bergen. K.X. acknowledges support in the form of a Ph.D. grant from the Chinese Scholarship Council. K.W.A.v.D. acknowledges support from the Delphi consortium for geo-imaging at TU Delft.

APPENDIX A: DISTORTED BORN APPROXIMATION

The distorted Born approximation can be derived as follows. First, we express integral Eq. (11) in operator form as

$$\psi = \psi^{(0)} + G^{(0)} V \psi. \tag{A1}$$

Then we compute the variation in the vectorial wavefield ψ due to a variation in the scattering potential V around a heterogeneous background medium where $V = V^{(b)}$ and $\psi = \psi^{(b)}$ and obtain

$$\delta\psi = G^{(0)} \delta V \psi^{(b)} + G^{(0)} V^{(b)} \delta\psi. \tag{A2}$$

By solving the above equation for the variation ψ, we obtain

$$\delta\psi = G^{(b)} \delta V \psi^{(b)}, \tag{A3}$$

where

$$\delta\psi = (I - G^{(0)} V^{(b)})^{-1} G^{(0)} \tag{A4}$$

is the Green's function $G^{(b)}$ for the heterogeneous medium with scattering potential $V^{(b)}$. If we now write down the above equation explicitly, we obtain

$$\delta\boldsymbol{\psi}(\mathbf{r}) = \int_M d^3x \mathbf{G}^{(b)}(\mathbf{r},\mathbf{x}) \cdot \delta\mathbf{V}(\mathbf{x}) \cdot \boldsymbol{\psi}(\mathbf{x}), \tag{A5}$$

which is the distorted Born approximation for the scattered vectorial wavefield in the real-space coordinate representation. Finally, we note that the matrix of modified Green's functions $\mathbf{G}^{(b)}(\mathbf{r},\mathbf{x})$ satisfies the usual reciprocity relations

$$G^{(b)}_{\alpha\beta}(\mathbf{r},\mathbf{x}) = G^{(b)}_{\beta\alpha}(\mathbf{x},\mathbf{r}), \quad \alpha,\beta = 1,2,3,4, \tag{A6}$$

which are important for matrix-free implementation of the adjoint integral equation method.

APPENDIX B: ADJOINT OPERATORS

The adjoint $\mathcal{F}_p^\dagger$ of the Fréchet derivative operator $\mathcal{F}_p$ is defined by

$$(\mathcal{F}_p^\dagger \Delta\boldsymbol{\psi}, \delta m)_M = (\Delta\boldsymbol{\psi}, F_p \delta m)_D, \tag{B1}$$

where $(,)_M$ and $(,)_D$ denote scalar products in the model and data spaces, respectively. By using the definition of the scalar products, we can rewrite Eq. (B1) more explicitly as

$$\int d^3x \left(\left[\mathcal{F}_p^\dagger \Delta\boldsymbol{\psi} \right](\mathbf{x}) \right)^* \delta m(\mathbf{x}) = \int d^3r d^3s \Delta\boldsymbol{\psi}^\dagger(\mathbf{r},\mathbf{s}) \cdot [\mathcal{F}_p \delta m](\mathbf{r},\mathbf{s}). \tag{B2}$$

https://doi.org/10.1121/10.0019563

By using the expression for $[\mathcal{F}_p \delta m](\mathbf{r},\mathbf{s})$ given in Eqs. (31) and (32) in conjunction with the above equation, we obtain

$$\begin{aligned}&\int d^3x \left(\left[\mathcal{F}_p^\dagger \Delta\boldsymbol{\psi} \right](\mathbf{x}) \right)^* \delta m(\mathbf{x}) \\ &= \int d^3r d^3s \Delta\boldsymbol{\psi}^\dagger(\mathbf{r},\mathbf{s}) \\ &\quad \cdot \int d\mathbf{x} \mathbf{G}^{(b)}(\mathbf{r},\mathbf{x}) \cdot \mathbf{B}^{(p)} \cdot \boldsymbol{\psi}^{(b)}(\mathbf{x},\mathbf{s}) \delta m(\mathbf{x}). \end{aligned} \tag{B3}$$

By rearranging the integrals on the right-hand side of the above equation, we obtain

$$\begin{aligned}&\int d^3x \left(\left[\mathcal{F}_p^\dagger \Delta\boldsymbol{\psi} \right](\mathbf{x}) \right)^* \delta m(\mathbf{x}) \\ &= \int d^3x \left[\int d^3r d^3s \Delta\boldsymbol{\psi}^\dagger(\mathbf{r},\mathbf{s}) \cdot \int d\mathbf{x} \mathbf{G}^{(b)}(\mathbf{r},\mathbf{x}) \right. \\ &\quad \left. \cdot \mathbf{B}^{(p)} \cdot \boldsymbol{\psi}^{(b)}(\mathbf{x},\mathbf{s}) \right] \delta m(\mathbf{x}). \end{aligned} \tag{B4}$$

Thus, it follows from the above equation that

$$\begin{aligned}\left(\left[\mathcal{F}_p^\dagger \Delta\boldsymbol{\psi} \right](\mathbf{x}) \right)^* &= \int d^3r d^3s \Delta\boldsymbol{\psi}^\dagger(\mathbf{r},\mathbf{s}) \cdot \int d^3x \mathbf{G}^{(b)}(\mathbf{r},\mathbf{x}) \\ &\quad \cdot \mathbf{B}^{(p)} \cdot \boldsymbol{\psi}^{(b)}(\mathbf{x},\mathbf{s}). \end{aligned} \tag{B5}$$

By using the reciprocity property $G^{(b)}_{\alpha\beta}(\mathbf{r},\mathbf{s}) = G^{(b)}_{\beta\alpha}(\mathbf{s},\mathbf{r})$, we get

$$\left(\left[\mathcal{F}_p^\dagger \Delta\boldsymbol{\psi} \right](\mathbf{x}) \right)^* = \boldsymbol{\psi}^{(a)} \cdot \mathbf{B}^{(p)} \cdot \boldsymbol{\psi}^{(b)}, \tag{B6}$$

where the adjoint field $\boldsymbol{\psi}^{(a)}$ is defined by

$$\boldsymbol{\psi}^{(a)}(\mathbf{x}) \equiv \int d^3r d^3s \mathbf{G}^{(b)}(\mathbf{x},\mathbf{r}) \cdot \Delta\boldsymbol{\psi}(\mathbf{r},\mathbf{s}). \tag{B7}$$

APPENDIX C: NONLINEAR CG METHOD

Model update in CG optimization method can be expressed as

$$\mathbf{m}_{k+1} = \mathbf{m}_k + \alpha_k \mathbf{p}_k, \tag{C1}$$

where α_k is the step length and $\mathbf{p}_k$ is the descent direction. The step length can be found from[50]

$$\alpha_k = \frac{\langle \mathcal{F}_k \mathbf{p}_k, \Delta\psi_k \rangle}{\langle \mathcal{F}_k \mathbf{p}_k, \mathcal{F}_k \mathbf{p}_k \rangle}, \tag{C2}$$

where $\mathcal{F}_k$ is the Fréchet derivative operator, and $\langle \cdot, \cdot \rangle$ is inner product. The descent direction $\mathbf{p}_k$ can be obtained as follows:[51]

$$\mathbf{p}_k = \begin{cases} -\mathbf{g}_1, & k = 1, \\ -\mathbf{g}_k + \gamma_k \mathbf{p}_{k-1}, & k > 1 \end{cases} \tag{C3}$$

in which

$$\mathbf{g}_k = \mathcal{F}_k^\dagger \Delta\psi_k. \tag{C4}$$

In Eq. (C3), γ_k is estimated from

$$\gamma_k = \max\left(0, \min\left(\gamma_k^1, \gamma_k^2\right)\right), \tag{C5}$$

where

$$\begin{cases} \gamma_k^1 = \dfrac{\langle \mathbf{g}_k, \mathbf{g}_k - \mathbf{g}_{k-1} \rangle}{\langle \boldsymbol{p}_{k-1}, \mathbf{g}_k - \mathbf{g}_{k-1} \rangle}, \\ \gamma_k^2 = \dfrac{\langle \mathbf{g}_k, \mathbf{g}_k \rangle}{\langle \boldsymbol{p}_{k-1}, \mathbf{g}_k - \mathbf{g}_{k-1} \rangle}. \end{cases} \tag{C6}$$

[1] R. G. Pratt, "Medical ultrasound tomography: Lessons from exploration geophysics," in *Proceedings of the 1st International Workshop on Medical Ultrasound Tomography*, Speyer, Germany (November 1–3, 2017), p. 65.

[2] A. B. Ramirez and K. W. van Dongen, "Can sources and receivers be interchanged for imaging?" in *Proceedings of the 2016 IEEE International Ultrasonics Symposium (IUS)*, Tours, France (September 18–21, 2016). pp. 1–4.

[3] C. Li, N. Duric, and L. Huang, "Clinical breast imaging using sound-speed reconstructions of ultrasound tomography data," in *Proceedings of Medical Imaging 2008: Ultrasonic Imaging and Signal Processing*, San Diego, CA (February 17–18, 2008), pp. 78–86.

[4] N. K. Martiartu, C. Boehm, and A. Fichtner, "3-D wave-equation-based finite-frequency tomography for ultrasound computed tomography," IEEE Trans. Ultrason. Ferroelectr. Freq. Control **67**(7), 1332–1343 (2020).

[5] L. Guasch, O. Calderón Agudo, M.-X. Tang, P. Nachev, and M. Warner, "Full-waveform inversion imaging of the human brain," npj Digit. Med. **3**(1), 28 (2020).

[6] G. Renaud, P. Kruizinga, D. Cassereau, and P. Laugier, "*In vivo* ultrasound imaging of the bone cortex," Phys. Med. Biol. **63**(12), 125010 (2018).

[7] R. H. Stolt and A. B. Weglein, *Seismic Imaging and Inversion* (Cambridge University, Cambridge, UK, 2012), Vol. 1.

[8] M. Jakobsen and B. Ursin, "Full waveform inversion in the frequency domain using direct iterative T-matrix methods," J. Geophys. Eng. **12**(3), 400–418 (2015).

[9] M. Jakobsen and R.-S. Wu, "Accelerating the T-matrix approach to seismic full-waveform inversion by domain decomposition," Geophys. Prospect. **66**(6), 1039–1059 (2018).

[10] N. Ozmen, R. Dapp, M. Zapf, H. Gemmeke, N. V. Ruiter, and K. W. van Dongen, "Comparing different ultrasound imaging methods for breast cancer detection," IEEE Trans. Ultrason. Ferroelectr. Freq. Control **62**(4), 637–646 (2015).

[11] U. Taskin, N. Ozmen, H. Gemmeke, and K. W. A. van Dongen, "Modeling breast ultrasound on the applicability of commonly made approximations," Arch. Acoust. **43**(3), 425–435 (2018).

[12] U. Taskin, K. S. Eikrem, G. Naevdal, M. Jakobsen, D. J. Verschuur, and K. W. Van Dongen, "Ultrasound imaging of the brain using full-waveform inversion," in *Proceedings of the 2020 IEEE International Ultrasonics Symposium (IUS)*, Las Vegas, NV (September 7–11, 2020).

[13] J. Bakker, M. Paulides, I.-M. Obdeijn, G. Van Rhoon, and K. Van Dongen, "An ultrasound cylindrical phased array for deep heating in the breast: Theoretical design using heterogeneous models," Phys. Med. Biol. **54**(10), 3201–3215 (2009).

[14] R. F. Remis and P. V. den Berg, "On the equivalence of the Newton–Kantorovich and distorted Born methods," Inverse Problems **16**(1), L1 (2000).

[15] R.-S. Wu, "Towards a theoretical background for strong-scattering inversion-direct envelope inversion and Gel'fand–Levitan–Marchenko theory," Commun. Comput. Phys. **28**, 41–73 (2020).

[16] R. W. Clayton and R. H. Stolt, "A Born-WKBJ inversion method for acoustic reflection data," Geophysics **46**(11), 1559–1567 (1981).

[17] R. H. Stolt and A. B. Weglein, "Migration and inversion of seismic data," Geophysics **50**(12), 2458–2472 (1985).

[18] A. B. Weglein, F. V. Araújo, P. M. Carvalho, R. H. Stolt, K. H. Matson, R. T. Coates, D. Corrigan, D. J. Foster, S. A. Shaw, and H. Zhang,

"Inverse scattering series and seismic exploration," Inverse Problems **19**(6), R27–R83 (2003).
[19]K. W. A. van Dongen and W. M. Wright, "A full vectorial contrast source inversion scheme for three-dimensional acoustic imaging of both compressibility and density profiles," J. Acoust. Soc. Am. **121**(3), 1538–1549 (2007).
[20]R. Lavarello and M. Oelze, "A study on the reconstruction of moderate contrast targets using the distorted Born iterative method," IEEE Trans. Ultrason. Ferroelectr. Freq. Control **55**(1), 112–124 (2008).
[21]M. Haynes and M. Moghaddam, "Large-domain, low-contrast acoustic inverse scattering for ultrasound breast imaging," IEEE Trans. Biomed. Eng. **57**(11), 2712–2722 (2010).
[22]U. Taskin and K. W. A. van Dongen, "Multi-parameter inversion with the aid of particle velocity field reconstruction," J. Acoust. Soc. Am. **147**(6), 4032–4040 (2020).
[23]J. Yang, Y. Liu, and L. Dong, "Simultaneous estimation of velocity and density in acoustic multiparameter full-waveform inversion using an improved scattering-integral approach," Geophysics **81**(6), R399–R415 (2016).
[24]A. J. Hesford and W. C. Chew, "A frequency-domain formulation of the Fréchet derivative to exploit the inherent parallelism of the distorted born iterative method," Waves Random Complex Media **16**(4), 495–508 (2006).
[25]A. J. Hesford and W. C. Chew, "Fast inverse scattering solutions using the distorted born iterative method and the multilevel fast multipole algorithm," J. Acoust. Soc. Am. **128**(2), 679–690 (2010).
[26]M. Jakobsen, E. Ivan, I. Psencik, and B. Ursin, "Transition operator approach to seismic full-waveform inversion in arbitrary anisotropic elastic media," Commun. Comput. Phys. **27**, 297–327 (2020).
[27]R. G. Pratt, C. Shin, and G. J. Hick, "Gauss–Newton and full Newton methods in frequency–space seismic waveform inversion," Geophys. J. Int. **133**(2), 341–362 (1998).
[28]L. Métivier, R. Brossier, S. Operto, and J. Virieux, "Second-order adjoint state methods for full waveform inversion," in *EAGE 2012—74th European Association of Geoscientistsand Engineers Conference and Exhibition*, Copenhagen, Denmark (June 4–7, 2012).
[29]J. Virieux and S. Operto, "An overview of full-waveform inversion in exploration geophysics," Geophysics **74**(6), WCC1–WCC26 (2009).
[30]S. C. Jun and U. Jin Choi, "Convergence analyses of the Born iterative method and the distorted Born iterative method," Numer. Funct. Anal. Optim. **20**(3–4), 301–316 (1999).
[31]A. B. Weglein, "A timely and necessary antidote to indirect methods and so-called P-wave FWI," Leading Edge **32**(10), 1192–1204 (2013).
[32]D. J. Kouri and A. Vijay, "Inverse scattering theory: Renormalization of the Lippmann–Schwinger equation for acoustic scattering in one dimension," Phys. Rev. E **67**(4), 046614 (2003).
[33]H. Zhang, "Direct non-linear acoustic and elastic inversion: Towards fundamentally new comprehensive and realistic target identification," Ph.D. thesis, University of Houston, Houston, TX, 2006.
[34]A. B. Weglein, F. A. Gasparotto, P. M. Carvalho, and R. H. Stolt, "An inverse-scattering series method for attenuating multiples in seismic reflection data," Geophysics **62**(6), 1975–1989 (1997).
[35]A. Weglein, F. Liu, X. Li, P. Terenghi, E. Kragh, J. D. Mayhan, Z. Wang, J. Mispel, L. Amundsen, H. Liang, L. Tang, and S.-Y. Hsu (2012). Inverse scattering series direct depth imaging without the velocity model: First field data examples. J. Seismic Explor. **21**, 1–28.
[36]Y. Zou and A. B. Weglein, "ISS Q compensation without knowing, estimating or determining Q and without using or needing low and zero frequency data," J. Seismic Explor. **27**, 593–608 (2018).
[37]H. Zhang and A. B. Weglein, "The inverse scattering series for tasks associated with primaries: Direct non-linear inversion of 1D elastic media," in *SEG Technical Program Expanded Abstracts 2006* (Society of Exploration Geophysicists, Houston, TX, 2006), pp. 2062–2066.
[38]A.-B. Weglein, "Direct and indirect inversion and a new and comprehensive perspective on the role of primaries and multiples in seismic data processing for structure determination and amplitude analysis," Ciencia Tecnologia Futuro **8**(2), 5–21 (2018).
[39]M. Jakobsen, R.-S. Wu, and X. Huang, "Convergent scattering series solution of the inhomogeneous Helmholtz equation via renormalization group and homotopy continuation approaches," J. Comput. Phys. **409**, 109343 (2020).
[40]M. Jakobsen, X. Huang, and R.-S. Wu, "Homotopy analysis of the Lippmann–Schwinger equation for seismic wavefield modelling in strongly scattering media," Geophys. J. Int. **222**(2), 743–753 (2020).
[41]V. Červený, *Seismic Ray Theory* (Cambridge University, Cambridge, UK, 2001).
[42]P. M. van den Berg, *Forward and Inverse Scattering Algorithms Based on Contrast Source Integral Equations* (Wiley, New York, 2021).
[43]K. Xiang, K. S. Eikrem, M. Jakobsen, and G. Nævdal, "Homotopy scattering series for seismic forward modelling with variable density and velocity," Geophys. Prosp. **70**, 3–18 (2021).
[44]C. G. Farquharson and D. W. Oldenburg, "A comparison of automatic techniques for estimating the regularization parameter in non-linear inverse problems," Geophys. J. Int. **156**(3), 411–425 (2004).
[45]R. C. Aster, B. Borchers, and C. H. Thurber, *Parameter Estimation and Inverse Problems* (Elsevier, Amsterdam, 2018).
[46]Ö. Yilmaz, *Seismic Data Analysis: Processing, Inversion, and Interpretation of Seismic Data* (Society of Exploration Geophysicists, Houston, TX, 2001).
[47]P. Zwamborn and P. M. van den Berg, "A weak form of the conjugate gradient FFT method for two-dimensional TE scattering problems," IEEE Trans. Microw. Theory Tech. **39**(6), 953–960 (1991).
[48]M. Jakobsen, "T-matrix approach to seismic forward modelling in the acoustic approximation," Stud. Geophys. Geod. **56**(1), 1–20 (2012).
[49]G. Gao, C. Torres-Verdin, and T. Habashy, "Analytical techniques to evaluate the integrals of 3D and 2D spatial dyadic Green's functions," Prog. Electromagn. Res. **52**, 47–80 (2005).
[50]A. Pica, J. Diet, and A. Tarantola, "Nonlinear inversion of seismic reflection data in a laterally invariant medium," Geophysics **55**(3), 284–292 (1990).
[51]W. W. Hager and H. Zhang, "A survey of nonlinear conjugate gradient methods," Pacific J. Optim. **2**(1), 35–58 (2006).